Influence of the surface states on the nonlinear Hall effect in Weyl semimetals

Diego García Ovalle,[*] Armando Pezo [ID],[†] and Aurélien Manchon [ID][‡]
Aix-Marseille Université, CNRS, CINaM, Marseille, France

We investigate the influence of surface states on the nonlinear Hall response driven by the Berry curvature dipole in non-centrosymmetric time-reversal invariant Weyl semimetals. To do so, we perform a tomography of the Berry curvature dipole in a slab system using a minimal two-band model. We find that in the type-I phase, the nonlinear Hall response is not particularly sensitive to the presence of Fermi arcs or other trivial surface states. However, in the type-II phase, we find that these surface states, be they topologically trivial or not, contribute substantially to the Berry curvature dipole, leading to a strong thickness dependence of the nonlinear Hall response. This feature depends on the nature of the surface states and, henceforth, on the slab geometry adopted. In order to assess the validity of this scenario for realistic systems, we performed Berry curvature dipole calculations by first principles on the WTe_2, confirming the dramatic impact of surface states for selected slab geometries. Our results suggest that surface states, being topological or not, can contribute much more efficiently to the nonlinear Hall response than bulk states. This prediction is not limited to topological semimetals and should apply to topologically trivial noncentrosymmetric materials and heterostructures, paving the way to interfacial engineering of the nonlinear Hall effect.

I. INTRODUCTION

Conventional wisdom inherited from Hall's foundational work [1,2] states that Hall currents flowing transverse to the injected charge direction are only permitted as long as time-reversal symmetry is globally broken. In other words, ordinary, anomalous, or topological Hall effects only exist either in the presence of an external magnetic field or in magnetic materials displaying a net magnetization [3]. However, this long-lived statement has been recently challenged by two important observations. First, it has been realized that anomalous Hall effect does not necessitate the presence of a *net* magnetic moment to exist. For instance, in an antiferromagnet the Hall effect can be nonzero as long as no crystal symmetry reinstalls the time-reversal effectively. This is particularly true for certain classes of antiferromagnets with a noncollinear magnetic configuration [4–7] (see also Ref. [8]). Second, the time-reversal symmetry breaking necessary to obtain Hall effect is not required anymore at the second order in the electric field. Under certain conditions, anomalous Hall effect can appear in nonmagnetic materials to the second order of the electric field [9–11]. Recently, it has been proposed that such a second-order Hall effect exists in collinear antiferromagnets where the linear Hall effect is absent, e.g., CuMnSb [12]. Whereas the intrinsic contribution to the linear anomalous Hall effect in ferromagnetic and antiferromagnetic compounds is associated with the Berry curvature of the material's ground state, the second-order, nonlinear anomalous Hall effect (NLHE) is rather associated with the Berry curvature dipole (BCD). From a symmetry standpoint, the minimal requirement is

inversion symmetry breaking which ensures that the Berry curvature does not vanish, but this is not sufficient: mirror symmetry also needs to be broken to obtain a finite BCD. Sodemann and Fu [9] identified the crystallographic point groups that possess the minimal requirements for the observation of NLHE, a study recently refined by Du *et al.* [13] to include both intrinsic (BCD related) and extrinsic mechanisms [14] allowed by symmetry.

Different material candidates have been explored experimentally and theoretically as suitable options to obtain NLHE. From an experimental point of view, quadratic responses in the electric field have been detected, among others, in bilayers and few layers of WTe_2 [10,11] which have C_{2v} point group. From a theoretical perspective, other possibilities for large BCD values have been proposed, including transition metal dichalcogenides [15–20], graphene [21–23], and especially Dirac [24] and Weyl semimetals (WSM) [25] (see also Ref. [26]). *Ab initio* simulations [27] have stimulated further theoretical studies of BCD in 3D WSMs, because of their rich geometrical features and their potential benefits to create highly efficient electronic transport devices. NLHE in WSMs has also been verified analytically by applying perturbation theory [28], suggesting that the transport is sensitive to intraband processes, the chemical potential and the tilting of the Weyl nodes. Besides, similar optical effects such as second harmonic generation can be confirmed by applying Floquet [29] and many-body quantum formalisms [30]. Last but not least, a full Green function theory of the NLHE has been proposed recently [13], pointing out the differences between extrinsic and intrinsic contributions. The former is associated with higher moments of the impurity potential whereas the latter is solely associated to the band structure. In this paper, we focus on the nonlinear response arising on the intrinsic mechanism driven by the BCD.

———————
[*]diego-fernando.garcia-ovalle@univ-amu.fr
[†]armando-arquimedes.pezo-lopez@univ-amu.fr
[‡]aurelien.manchon@univ-amu.fr

Nonmagnetic WSMs such as TaAs or WTe$_2$ are particularly interesting platforms for the realization of NLHE because inversion symmetry is necessarily broken and Berry curvature diverges at the Weyl nodes. WSMs possess pairs of doubly degenerate linearly dispersive states, forming Weyl cones at Fermi level [31]. According to the Nielsen-Ninomiya theorem [32], each pair of nodes carries Berry curvature monopoles of opposite chirality which are connected via Fermi arcs lying at opposite surfaces of the slab [33]. Type-I WSMs, such as elemental Tellurium [34], Janus superlattices [35] and Ta or As compounds [36–38], are characterized by pointlike Fermi surface in the bulk and vanishing density of states. Type-II WSMs, such as MoTe$_2$ [39,40] and WTe$_2$ [41,42] but also the magnetic candidate Co$_3$Sn$_2$S$_2$ [43–48], offer a slightly different paradigm as the Weyl cone spectrum is tilted in momentum space, breaking Lorentz invariance. As a result, the Weyl points arise at the boundary between electron and hole pockets. Notice that certain compounds can support type-I as well as type-II Weyl nodes [49,50].

A remarkable aspect of WSMs is the nature of their surface states. As mentioned above, alike topological insulators WSMs possess topologically protected surface states in the form of spin-momentum locked Fermi arcs that connect bulk Weyl nodes of opposite chirality. In type-I WSMs, the Fermi arcs coexist with the projection of electron (or hole) pockets when the chemical potential lies away from the neutrality point. In type-II WSMs, the Fermi arcs coexist with projected electron and hole pockets irrespective of the value of the chemical potential, as well as with trivial closed loops called "track states" [51]. As a consequence, surface states of WSMs can be rich, resulting in enhanced Edelstein effect [52], and unconventional patterns in quantum oscillation experiments [53–55] (see also Ref. [56]). Previous works pointed out that topological materials defined in slab geometries can exhibit interesting transport properties due to finite size effects and the behavior of surface states inside the samples. In this context, it has been shown that the anomalous Hall conductivity is highly influenced by surface states such as Fermi arcs in Weyl systems without time-reversal symmetry [57], even in presence of disorder [58]. Additional studies have been performed in confined geometries to clarify, among others, the behavior of chiral magnetic effects [59], the magnetoresistance [60], and the quantum Hall effect in Dirac semimetals [61].

In this work, we seek to understand how the surface states of nonmagnetic WSMs influence the NHLE response driven by the BCD. To do so, we consider a minimal two-band model of a time-reversal invariant WSM with inversion symmetry breaking in a slab geometry, so that bulk and surface states are treated on equal footing [51]. This model exhibits four Weyl points: the minimum number of degeneracies due to time-reversal symmetry. These four points are associated with local divergencies of the Berry curvature, as depicted on Fig. 1. In this sense, after neglecting the vanishing components of the BCD tensor due to mirror symmetries in the 3D lattice, Zeng *et al.* [25] recently reported that NLHE requires Weyl cone tilting and an asymmetric Fermi surface when the nodes lie at the same energy. The NLHE is also influenced by the distance between nodes. Accordingly, our study gives further insight about the implications of the Fermi arc configurations on the BCD. Remarkably, it also complements a recent study that
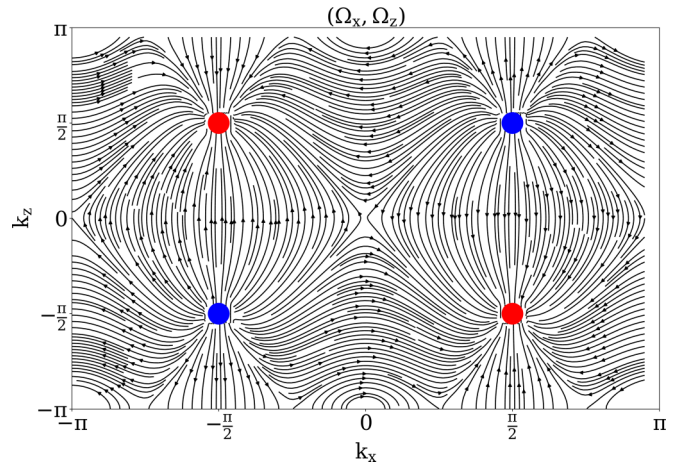

FIG. 1. Berry curvature of the Hamiltonian (4) in the (k_x, k_z) plane with $k_y = 0$ and intrinsic parameters $k_0 = \frac{\pi}{2}$, $m = 2$, $t_x = \frac{1}{2}$, $\gamma = 1$, and $t = 1$. Note that the Berry curvature of the two-band model is not sensitive to the value of γ [51]. The solid lines represent the Berry curvature vector field (Ω_x, Ω_z), whereas the blue (red) dots represent the local positive (negative) divergencies taking place at the Weyl nodes.

comprises a surface BCD due to the projection of Fermi arcs in type-I WSMs [62].

Our paper is organized as follows. In Sec. II, we recall the general formalism for nonlinear Hall transport driven by BCD and basic physical considerations for our model of interest. In Sec. III, we provide and discuss our results regarding the connection between surface states and NLHE, its dependency on the Weyl cones tilting and its layer decomposition. In Sec. IV, we also collate these outcomes with realistic numerical simulations on a WTe$_2$ slab with different cuts. Finally, we summarize and state our main conclusions in Sec. V.

II. GENERAL THEORY AND MODEL

Let us begin by recalling basic elements of NLHE theory [9]. We start with a nonmagnetic crystal and its corresponding Bloch Hamiltonian $\mathcal{H}_\mathbf{k}$, whose eigenstates $|u_{n\mathbf{k}}\rangle$ satisfy Schrödinger equation $\mathcal{H}_\mathbf{k} |u_{n\mathbf{k}}\rangle = \epsilon_{n\mathbf{k}} |u_{n\mathbf{k}}\rangle$ with eigenenergies $\epsilon_{n\mathbf{k}}$. If the crystal is subjected to a sufficiently small electric field $\mathbf{E} = \text{Re}[\mathcal{E} \exp(i\omega t)]$, $\mathcal{E} \in \mathbb{C}^3$, such that the adiabatic limit is still valid, and assuming weak disorder, the first order Hall current is induced by the Berry curvature [3]

$$\mathbf{\Omega}_{n\mathbf{k}} = i \sum_{m \neq n} \frac{\langle u_{n\mathbf{k}} | \hat{\mathbf{v}}_\mathbf{k} | u_{m\mathbf{k}} \rangle \times \langle u_{m\mathbf{k}} | \hat{\mathbf{v}}_\mathbf{k} | u_{n\mathbf{k}} \rangle}{(\epsilon_{n\mathbf{k}} - \epsilon_{m\mathbf{k}})^2}, \quad (1)$$

where $\hat{\mathbf{v}}_\mathbf{k} = \partial_\mathbf{k} \mathcal{H}_\mathbf{k}$ is the velocity operator. Upon time reversal operation $\mathcal{T}$ we have $\mathcal{T}\mathbf{\Omega}_{n\mathbf{k}}\mathcal{T}^{-1} = -\mathbf{\Omega}_{n-\mathbf{k}}$, and thus the anomalous Hall effect vanishes. Nonetheless, when inversion symmetry $\mathcal{P}$ is further broken, then $\mathcal{P}\mathbf{\Omega}_{n\mathbf{k}}\mathcal{P}^{-1} \neq \mathbf{\Omega}_{n-\mathbf{k}}$, and one can show to the lowest order in scattering time τ, that the (rectified) second order Hall current reads [9]

$$j_a^0 = \left(\frac{e^3\tau}{2\hbar^2}\right)\epsilon_{adc}D_{bd}\mathcal{E}_b\mathcal{E}_c^*. \quad (2)$$

Here, latin indices refer to the components of the usual Cartesian basis and ϵ_{adc} is the Levi-Civita tensor. D_{bd} is the BCD defined as [9]

$$D_{bd} = \int_{BZ} \frac{d^3\mathbf{k}}{(2\pi)^3} \left[\sum_n (\mathbf{v}_{n\mathbf{k}})_b (\mathbf{\Omega}_{n\mathbf{k}})_d \frac{\partial f_{n\mathbf{k}}}{\partial \epsilon_{n\mathbf{k}}} \right], \qquad (3)$$

with $\mathbf{v}_{n\mathbf{k}} = \partial_{\mathbf{k}} \epsilon_{n\mathbf{k}}$ the eigenvalues of the velocity operator and $f_{n\mathbf{k}}$ the Fermi distribution function. In the zero-temperature limit, $\partial_{\epsilon_{n\mathbf{k}}} f_{n\mathbf{k}} \rightarrow -\delta(\epsilon_{n\mathbf{k}} - \mu)$, setting μ as the chemical potential. Equation (2) neglects the intrinsic contribution to NLHE that appears when time reversal is broken as well as higher order extrinsic contributions (i.e., side-jump and skew scattering) [13,14].

The nonmagnetic WSM slab is built on the spinless two-band model in a cubic lattice introduced in Ref. [51]. The bulk Hamiltonian reads

$$\mathcal{H}_B = \gamma(\cos 2k_z - \cos k_0)(\cos k_x - \cos k_0)\hat{\sigma}_0$$
$$- [m(1 - \cos^2 k_x - \cos k_y) + 2t_x(\cos k_z - \cos k_0)]\hat{\sigma}_1$$
$$- 2t \sin k_y \hat{\sigma}_2 - 2t \cos k_x \hat{\sigma}_3, \qquad (4)$$

with $\hat{\sigma}_i$, $i = 1, \ldots, 3$ being the 2×2 Pauli matrices, $\hat{\sigma}_0 = \mathbb{1}_{2\times2}$ and the cubic Brillouin zone is $\mathcal{C} = [-\pi, \pi]^3$. The parameters of Eq. (4) are set to $k_0 = \frac{\pi}{2}$, $m = 2$, $t_x = \frac{1}{2}$, and $t = 1$. This WSM possesses four Weyl nodes of zero energy located at $\mathbf{k}^* = \pm\frac{\pi}{2}(\hat{x} + \hat{z})$ (see Fig. 1). Importantly, for the parameters adopted in this work, $\gamma = 2$ sets the transition point between type-I ($\gamma < 2$) and type-II ($\gamma > 2$) WSM phases. In the remaining of this paper, the transport properties will be investigated as a function of the chemical potential μ as well as of the tilting of the Weyl cones controlled by γ. Interestingly, Eq. (4) is constrained by the following mirror symmetries [25]:

$$\mathcal{M}_x^\dagger \mathcal{H}_B(k_x, k_y, k_z)\mathcal{M}_x = \mathcal{H}_B(-k_x, k_y, k_z), \qquad (5)$$

$$\mathcal{M}_z^\dagger \mathcal{H}_B(k_x, k_y, k_z)\mathcal{M}_z = \mathcal{H}_B(k_x, k_y, -k_z), \qquad (6)$$

which impose that the Fermi arcs connecting the Weyl nodes lie on the (z, x) surfaces. In addition, these symmetries constrain the BCD tensor, so that the only nonvanishing elements are D_{zx} and D_{xz}. In other words, a second order Hall current can only be obtained in the $(y, z) (\equiv D_{zx})$ and $(x, y) (\equiv D_{xz})$ planes. Consequently, the Fermi arcs cannot contribute to the NLHE response. Nevertheless, as discussed below, other trivial surface states can substantially impact the second order response.

We now design the slabs by discretizing Eq. (4) along a given direction, $\hat{x}$, $\hat{y}$, or $\hat{z}$, of the cubic Brillouin Zone (see, e.g., Ref. [63]). The Hamiltonian loses periodicity along the chosen axis. The new Hamiltonian $\mathcal{H}_S^{\hat{n}}$ of size $2L\times2L$, with $\hat{n} = \hat{x}$, $\hat{y}$, $\hat{z}$ depending on the growth direction, and L the

number of layers, is given by

$$\mathcal{H}_S^{\hat{n}} = \begin{pmatrix} \mathcal{H}_0^{\hat{n}} & \mathcal{H}_1^{\hat{n}} & \mathcal{H}_2^{\hat{n}} & 0 & \cdots & 0 \\ \mathcal{H}_1^{\hat{n}\dagger} & \mathcal{H}_0^{\hat{n}} & \mathcal{H}_1^{\hat{n}} & \mathcal{H}_2^{\hat{n}} & \ddots & \vdots \\ \mathcal{H}_2^{\hat{n}\dagger} & \mathcal{H}_1^{\hat{n}\dagger} & \ddots & \ddots & \ddots & 0 \\ 0 & \mathcal{H}_2^{\hat{n}\dagger} & \ddots & \ddots & \ddots & \mathcal{H}_2^{\hat{n}} \\ \vdots & \ddots & \ddots & \ddots & \ddots & \mathcal{H}_1^{\hat{n}} \\ 0 & \cdots & 0 & \mathcal{H}_2^{\hat{n}\dagger} & \mathcal{H}_1^{\hat{n}\dagger} & \mathcal{H}_0^{\hat{n}} \end{pmatrix}. \quad (7)$$

For the block matrices in Eq. (7), $\mathcal{H}_0^{\hat{n}}$ is the intralayer Hamiltonian that retains in-plane periodicity after the cut, while $\mathcal{H}_1^{\hat{n}}$ and $\mathcal{H}_2^{\hat{n}}$ are the nearest neighbor and second nearest neighbor interlayer Hamiltonian, respectively. For the cut along $\hat{x}$, the block matrices are given by

$$\mathcal{H}_0^{\hat{x}} = -\gamma \cos k_0(\cos 2k_z - \cos k_0)\hat{\sigma}_0$$
$$- \left[m\left(\frac{1}{2} - \cos k_y\right) + 2t_x(\cos k_z - \cos k_0) \right]\hat{\sigma}_1$$
$$- 2t \sin k_y \hat{\sigma}_2, \qquad (8)$$

$$\mathcal{H}_1^{\hat{x}} = \frac{\gamma}{2}(\cos 2k_z - \cos k_0)\hat{\sigma}_0 - t\hat{\sigma}_3, \qquad (9)$$

$$\mathcal{H}_2^{\hat{x}} = \frac{m}{4}\hat{\sigma}_1. \qquad (10)$$

A cut along $\hat{y}$ leads to

$$\mathcal{H}_0^{\hat{y}} = \gamma(\cos 2k_z - \cos k_0)(\cos k_x - \cos k_0)\hat{\sigma}_0$$
$$- [m \sin^2 k_x + 2t_x(\cos k_z - \cos k_0)]\hat{\sigma}_1$$
$$- 2t \cos k_x \hat{\sigma}_3, \qquad (11)$$

$$\mathcal{H}_1^{\hat{y}} = \frac{m}{2}\hat{\sigma}_1 + it\hat{\sigma}_2. \qquad (12)$$

Finally, a cut along $\hat{z}$ gives

$$\mathcal{H}_0^{\hat{z}} = -\gamma \cos k_0(\cos k_x - \cos k_0)\hat{\sigma}_0$$
$$- [m(1 - \cos^2 k_x - \cos k_y) - 2t_x \cos k_0]\hat{\sigma}_1$$
$$- 2t \sin k_y \hat{\sigma}_2 - 2t \cos k_x \hat{\sigma}_3, \qquad (13)$$

$$\mathcal{H}_1^{\hat{z}} = -t_x \hat{\sigma}_1, \qquad (14)$$

$$\mathcal{H}_2^{\hat{z}} = \frac{\gamma}{2}(\cos k_x - \cos k_0)\hat{\sigma}_0. \qquad (15)$$

We illustrate the slab band structures for each cut in Fig. 2, for $\gamma = 1$ (type-I WSM) and $\gamma = 3$ (type-II WSM). Since the slab Hamiltonians retain a Berry curvature perpendicular to the plane of the slab, we define $D_{zx}^{\hat{x}}$ as the BCD associated with $\mathcal{H}_S^{\hat{x}}$ when the electric field is applied along $\hat{z}$, and $D_{xz}^{\hat{z}}$ is the BCD associated with $\mathcal{H}_S^{\hat{z}}$ when the electric field is along $\hat{x}$. These are the only relevant BCD components for the slab geometries presented above due to the symmetry restrictions. We now move forward to the method for calculating the layer decomposition of transport coefficients in the slabs. Since the periodic part of the Bloch function can be written in terms of the complete layer basis as $|u_{n\mathbf{k}}\rangle = \sum_{l=1}^{L} |\omega_{l\mathbf{k}}\rangle \langle \omega_{l\mathbf{k}}|u_{n\mathbf{k}}\rangle$, one can extract information about layer l by applying the projection operator $\mathcal{S}_l = |\omega_{l\mathbf{k}}\rangle \langle \omega_{l\mathbf{k}}|$, $l \in [1, L]$ to an observable $\mathcal{O}$. In this way, it is easy to see that $\mathcal{O} = \sum_{l=1}^{L} \mathcal{S}_l \mathcal{O}$ and $\sum_{l=1}^{L} \mathcal{S}_l = \mathbb{1}_{2L\times2L}$. We use this description to separate the
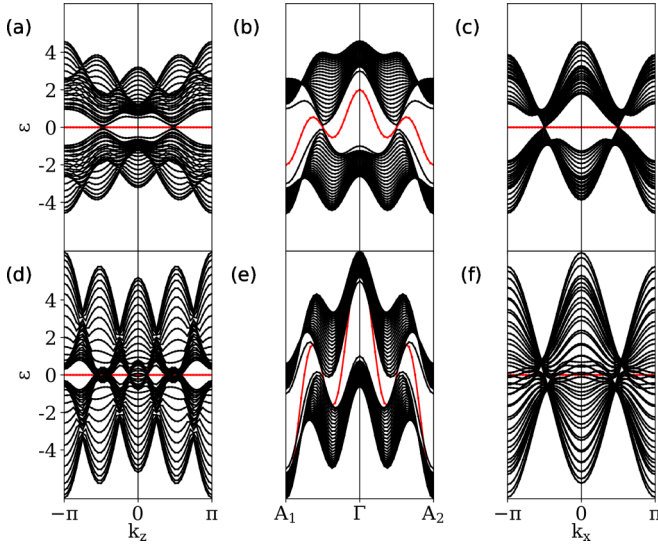
FIG. 2. Band structures of the WSM slab of 25 layers, with $\gamma = 1$ [(a)–(c)] and $\gamma = 3$ [(d)–(f)] along the high symmetry path of the cubic lattice for different cuts: (left panels) $\hat{x}$ for $k_y = 0$ and $k_z \in [-\pi, \pi]$, (center) $\hat{y}$ along the path $A_1 = (-\pi, 0, -\pi) \rightarrow \Gamma = (0, 0, 0) \rightarrow A_2 = (\pi, 0, \pi)$ and (right) $\hat{z}$ for $k_y = 0$ and $k_x \in [-\pi, \pi]$. The central panels clearly displays type-I (b) and type-II (e) Weyl cones. The surface states at the top and bottom surfaces are represented with a solid red line. The flat red bands in (a), (c), (d), and (f) are surface states at zero energy that are highly localized at the corresponding surfaces.

contributions of the density of states for a slab with a fixed number of layers,

$$\mathcal{D}_{l\mathbf{k}} = -\frac{1}{\pi} \operatorname{Im} \left[\operatorname{Tr} \left(\mathcal{S}_l G_{\mathbf{k}}^{\mathrm{R}} \right) \right], \qquad (16)$$

with the retarded Green's function

$$G_{\mathbf{k}}^{\mathrm{R}} = \lim_{\eta \to 0^+} \left[(\epsilon + i\eta) \mathbb{1} - \mathcal{H}_S^{\hat{n}} \right]^{-1}. \qquad (17)$$

This decomposition provides an insight about the influence of the surface states for each growth direction. Additionally, in order to obtain the contribution of layer l to the NLHE response along, say, $\hat{y}$, one simply needs to perform the substitution $\hat{v}_y \rightarrow \mathcal{S}_l \hat{v}_y$ into Eq. (1) and then into (3).

III. RESULTS AND DISCUSSION

A. Band structure and surface states

Let us first consider how the Weyl cone tilting impacts the slab band structure and its surface states. Since only $D_{zx}^{\hat{x}}$ and $D_{xz}^{\hat{z}}$ are nonvanishing, and because the Weyl nodes are located in the (k_x, k_z) plane, we focus on slabs composed of $L = 25$ layers and normal to the $\hat{x}$ and $\hat{z}$ directions. Without loss of generality, we fix the chemical potential to $\mu = 0.2$ and select the exemplary cases $\gamma = 1$, 3 to illustrate the differences between a type-I and a type-II WSM, respectively. To better understand how bulk and surface states evolve upon tilting the Weyl cones, we represent the density of states in the 2D Brillouin zone and projected on a set of representative layers, ranging from the bottommost surface to the topmost surface.

Our results are depicted in Figs. 3(a) and 3(c) for the $\hat{x}$ cut and Figs. 3(b) and 3(d) for the $\hat{z}$ cut.

Figures 3(a), 3(c) and 3(b), 3(d) show different behaviors of the bulk and surface states when tuning the tilting parameter. When $\hat{n} = \hat{x}$ [Figs. 3(a) and 3(c)], notice two distinct situations depending on the value of γ: if $\gamma = 1$ [type-I, Fig. 3(a)], the density of states is dominated by the Weyl nodes across the whole slab, with a surface state composed of the projected nodes connected by degenerate Fermi arcs. When $\gamma = 3$, [type-II, Fig. 3(c)], the density of states of the central layer is composed of electron and hole pockets touching at the Weyl nodes, as expected. These pockets result in large trivial surface Fermi pockets enclosing the nodes, whose connections change direction from $\hat{z}$ (type-I) to $\hat{x}$ (type-II) WSMs [51]. A map of the Fermi arcs' reconnection and surface states' evolution as a function of the tilting γ can be found in Appendix A.

On the other hand, for $\hat{n} = \hat{z}$ [Figs. 3(b) and 3(d)], we obtain a different behavior. Whereas for $\gamma = 1$ [type-I, Fig. 3(b)], the Weyl nodes remain disconnected throughout the slab, for $\gamma = 3$ [type-II, Fig. 3(d)], a surface contribution appears due to the emergence of track states [51]. Nonetheless, the surface Fermi pockets associated with the projection of the bulk electron and hole pockets remain very small and the surface states are dominated by the Weyl nodes, in sharp contrast with the $\hat{x}$ cut discussed in Figs. 3(a) and 3(c). We therefore expect the surface states to have completely different impact on the NLHE signal in these two different slab geometries.

B. Nonlinear Hall response

Let us now turn our attention towards the NLHE response for the two slabs. We compute the BCD components given by Eq. (4) in both slab geometries, (a) $D_{zx}^{\hat{x}}/L$ ($\hat{x}$ cut) and (b) $D_{xz}^{\hat{z}}/L$ ($\hat{z}$ cut), as well as in the 3D bulk structure, $D_{zx(xz)}^{\mathrm{3D}}$ (black symbols), in order to better identify the impact of the surface states. Notice that the BCD calculated in the slab geometry is normalized by the number of layers L to allow for a quantitative comparison with the BCD calculated in the bulk. By definition, the BCD is therefore unitless. In the following, we set the chemical potential to $\mu = 0.2$ and represent the BCDs as a function of the tilting parameter γ, as displayed in Figs. 4(a) and 4(b). In addition, the corresponding ratio between the BCD and the density of states is reported on Figs. 4(c) and 4(d) and discussed further below.

For the $\hat{x}$ cut [Fig. 4(a)], the bulk BCD (D_{zx}^{3D}, black symbols) displays a nonlinear dependence as a function of the tilting parameter, as observed by Zeng *et al.* [25]: it first increases smoothly with γ, reaches a maximum and decreases for large γ. We attribute this tendency to the contribution of the Fermi surface between the Weyl nodes, as also mentioned by Zeng *et al.* [25], and the upper limit that should reach the tilting parameter regarding the inclination of the Weyl nodes. In contrast, the slab BCD ($D_{zx}^{\hat{x}}$, colored symbols) increases sharply and reaches a plateau at large γ. Furthermore, the value of this plateau is substantially larger than the maximum value obtained in the bulk although it slightly decreases when increasing the number of layers, suggesting that surface states play a major role in the NLHE response. Since the transition between type-I and type-II regimes produces a change in the
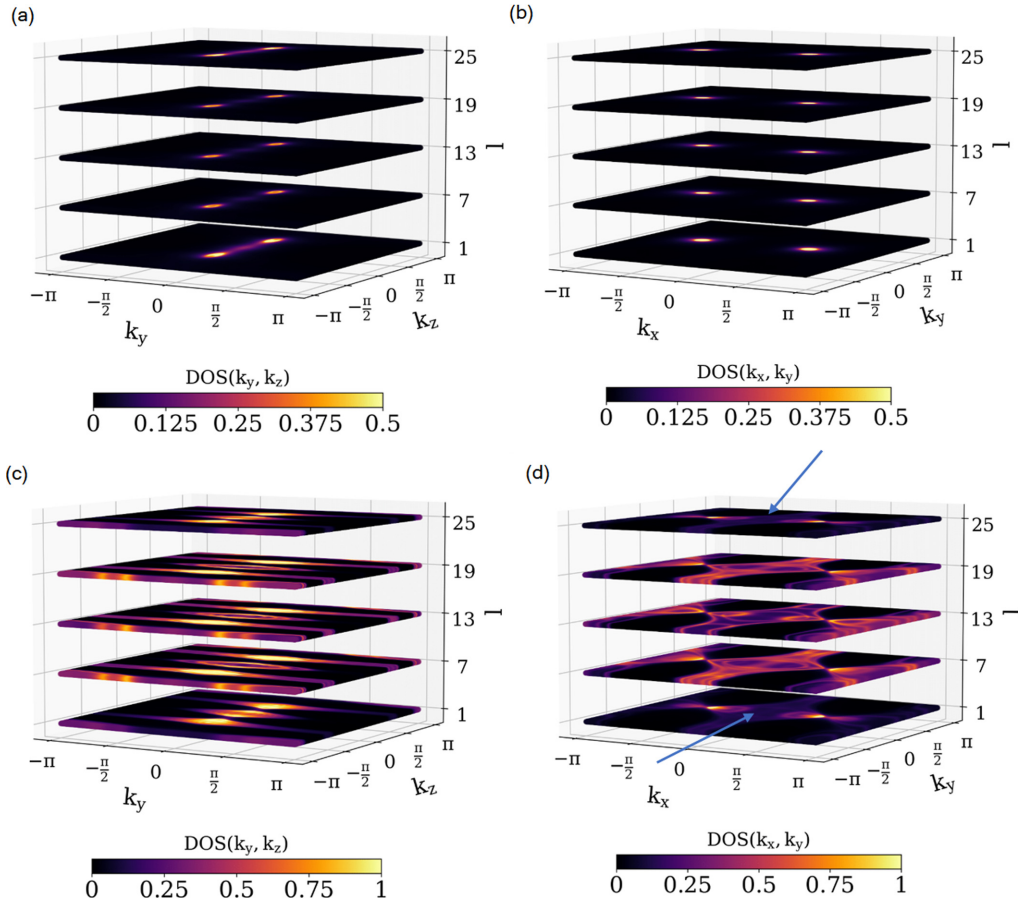
FIG. 3. Projected density of states (DOS) for [(a) and (c)] $\hat{n} = \hat{x}$ and [(b) and (d)] $\hat{n} = \hat{z}$ as a function of the momentum coordinates for selected layers l for the type-I ($\gamma = 1$) [(a) and (b)] and type-II ($\gamma = 3$) phases [(b) and (d)]. For the $\hat{x}$ cut in the type-I phase (a), the Weyl nodes dominate in the bulk and get connected by degenerate Fermi arcs at the surface, whereas in the type-II phase (c), large trivial Fermi pockets appear across the slab. For the $\hat{z}$ cut in the type-I phase (b), the Weyl nodes remain disconnected across the slab, whereas in the type-II phase (d), trivial Fermi pockets dominate in the bulk with track states and projected Weyl nodes at the surface. The track states' projections are centered around $k_x = 0, \pm\pi$, which are indicated with blue arrows on each corresponding layer.

configuration of the surface states, with the apparition of large Fermi pockets [Fig. 3(c)], it is clear that the mismatch between the slab and bulk responses arise from the influence of the Fermi pockets' projections on the BCD across the slab.

Conversely, for the $\hat{z}$ cut [Fig. 4(b)], the bulk and slab BCDs show a similar behavior, increasing continuously and displaying local plateaus at the type-I–type-II transition, as well as for large tilting parameter γ. Based on Fig. 3(d), we infer that the surface track states and other trivial states do not affect qualitatively the behavior of BCD in finite slab samples. In fact, in the $\hat{z}$ cut, the slab BCD converges faster towards the bulk BCD when increasing the number of layers than in the $\hat{x}$-cut configuration.

Since the density of states of carriers also changes when tuning the band structure, we report the corresponding ratio between the BCD and the density of states in Figs. 4(c) and 4(d). In Fig. 4(c), for a slab normal to $\hat{x}$, the renormalized BCD exhibits a qualitatively similar trend across the type-I-to-type-II transition, although the slab BCD is markedly larger than the bulk BCD when approaching the type-II regime. Therefore the Fermi pockets' projections on this slab enhance the value of the BCD due to the reconfiguration of the surface states and the presence of more local states within the unit cell. In

contrast, for a slab normal to $\hat{z}$ in Fig. 4(d) shows a smaller discrepancy between the slab and bulk calculations suggesting that the BCD is weakly impacted by the track states and other trivial states.

The calculations displayed in Fig. 4 have been performed at $\mu = 0.2$. Looking a the band structures in Fig. 2, one expects the relative contribution of bulk and surface states to the NLHE to vary when increasing the chemical potential. In particular, when μ leaves the regions of the Weyl cones, the bulk states should dominate the transport. Nonetheless, as further discussed in Appendix B, we find that as long as the chemical potential lies close to the Weyl cones, the distinct behavior of the BCD in the two different slabs, x cut and z cut, is qualitatively the same in the type-II regime: the surface states substantially contribute to the nonlinear transport for the x cut, whereas they are negligible in the z cut. To complement this analysis, we compute the layer decomposition of the NLHE in slab geometries, for $\gamma = 1$, 3 and $L = 25$. The result is reported in Fig. 5 for (a) $\gamma = 1$ and (b) $\gamma = 3$ for $\hat{x}$ (black) and $\hat{z}$ cut (red). As we can see from Fig. 5(a), in a type-I WSM the NLHE response strongly differs at the edges, i.e, at the top ($l = 1$) and bottom ($l = 25$) layers. From Figs. 3(a) and 3(b), we attribute this behavior to the surface states driven by the
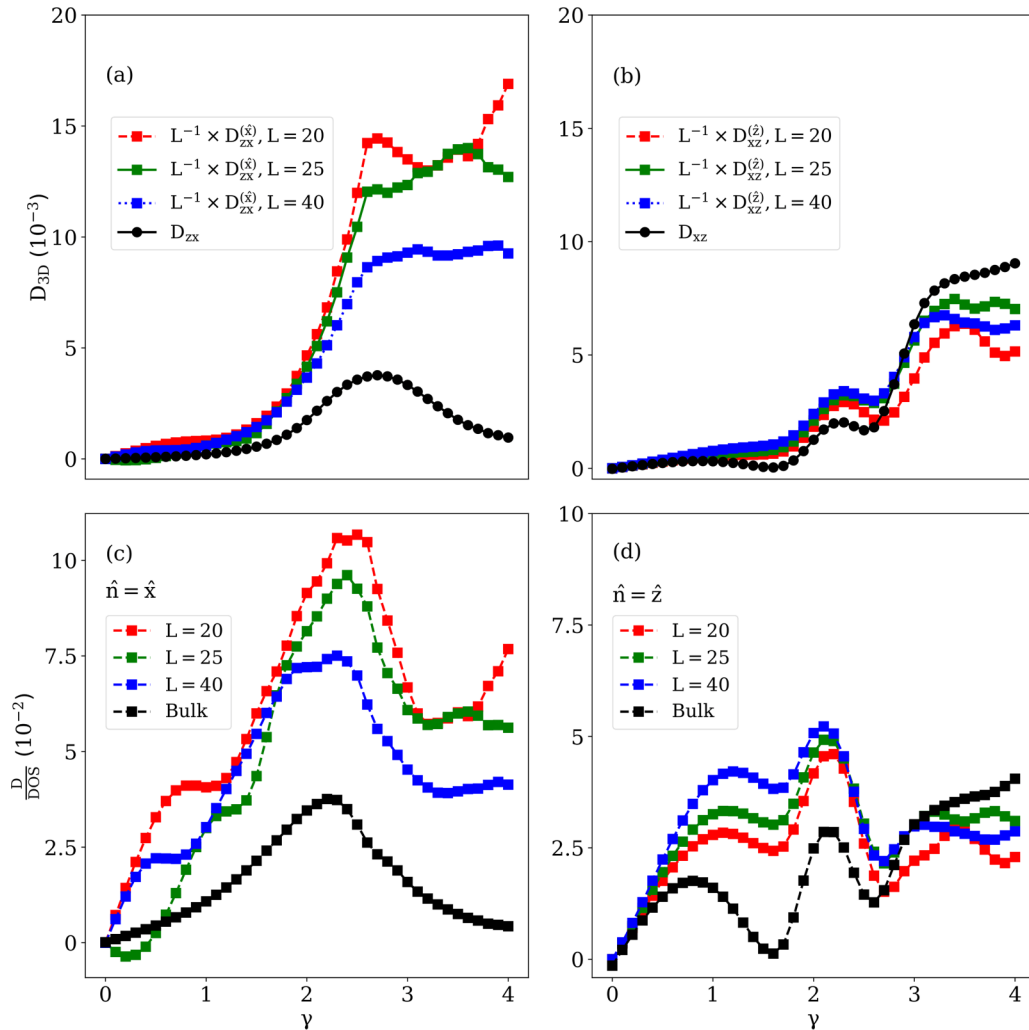
FIG. 4. BCD components as a function of the tilting parameter γ for slab and bulk systems. (a) Slab ($D_{zx}^{\hat{x}}/L$) and bulk (D_{zx}^{3D}) components for the $\hat{x}$ cut, for different slab thicknesses. (b) Slab ($D_{xz}^{\hat{z}}/L$) and bulk (D_{xz}^{3D}) components for the $\hat{z}$ cut, for different slab thicknesses. [(c) and (d)] Corresponding ratio between the BCD coefficient and the corresponding density of states for bulk and slab systems for the $\hat{x}$ cut (c) and $\hat{z}$ cut (d).

degenerate Fermi arcs that only appear in the $\hat{x}$ cut. In the case of the type-II WSM, Fig. 5(b), we note that the magnitude of the central layer ($l = 13$) in the $\hat{x}$ cut is larger than that in the $\hat{z}$ cut. Actually, the main contributions stem from layers located underneath the surfaces ($l = 5$, $l = 21$) rather than on the surface layers. This fact corroborates our claim that in type-II WSMs a decisive factor to enhance NLHE is the presence of Fermi pockets' projections at the surface rather than track states. It is worth mentioning that as long as the surface states are topologically protected (i.e., Fermi arcs), a weak influence of surface disorder is expected. Nonetheless, topologically trivial states, such as the ones that contribute the most to the NLHE in our study, are more sensitive to surface disorder, which should impact their overall response. We leave this observation to further studies.

Finally, let us comment on the experimental signature of the surface contribution to the NLHE. Based on the analysis provided above, it is clear that the surface states contribute substantially to the overall signal in the $\hat{x}$ cut, whereas it contributes marginally to the signal in the $\hat{z}$ cut. As a con-

sequence, one expects a strong difference between these two slabs when measuring the NLHE as a function of the thickness. Figure 6 displays the thickness dependence of the NLHE in a type-II WSM calculated at $\mu = 0.2$ and $\gamma = 3$, in both $\hat{z}$ cut (blue) and $\hat{x}$ cut (red). Whereas the NLHE of both slabs converge towards the bulk values at large thicknesses (dashed lines), they exhibit a distinct behavior at small thicknesses. In the $\hat{x}$ cut where the surface states contribute massively to the NLHE (see Fig. 4), the signal increases substantially at small thicknesses, whereas in the $\hat{z}$ cut, no such behavior is reported. This distinct feature can be used as an indication of surface state-driven NLHE in experiments.

IV. NONLINEAR HALL EFFECT IN WTe₂ SLABS

Let us now consider a realistic system, WTe$_2$ in its orthorhombic phase, and compute the NLHE from first principles. WTe$_2$ is a well-known type-II WSM [41,42], in which NLHE has been originally reported [10,11]. For the density functional theory simulations [64,65], we used the
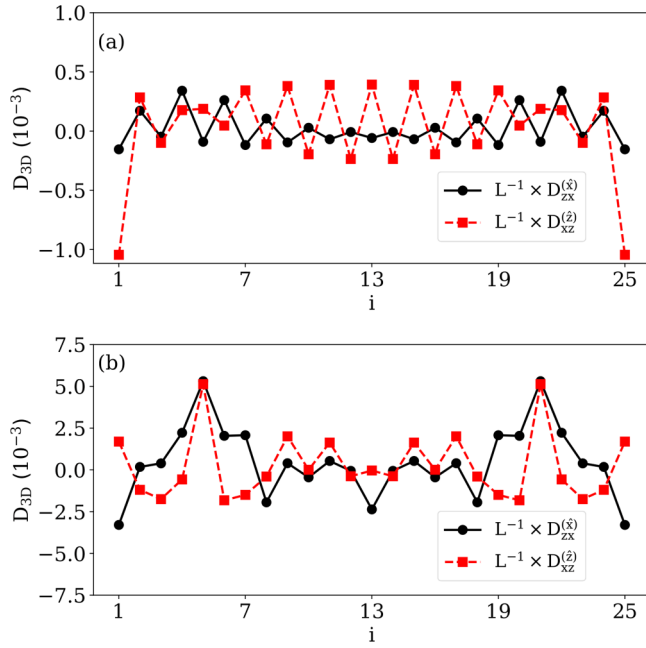
FIG. 5. Layer dependent contribution for the BCD normalized by the number of layers (in this case, $L = 25$). We show the tomography for a type-I WSM with $\gamma = 1$ in (a) and for a type-II WSM with $\gamma = 3$ in (b).

Perdew-Burke-Ernzerhof [66,67] exchange-correlation functional. The geometry optimizations were performed using a plane-wave basis as implemented in the Vienna *ab initio* simulation package (VASP) [68,69]. We have employed 400 eV for the plane-wave expansion cutoff with a force criterion
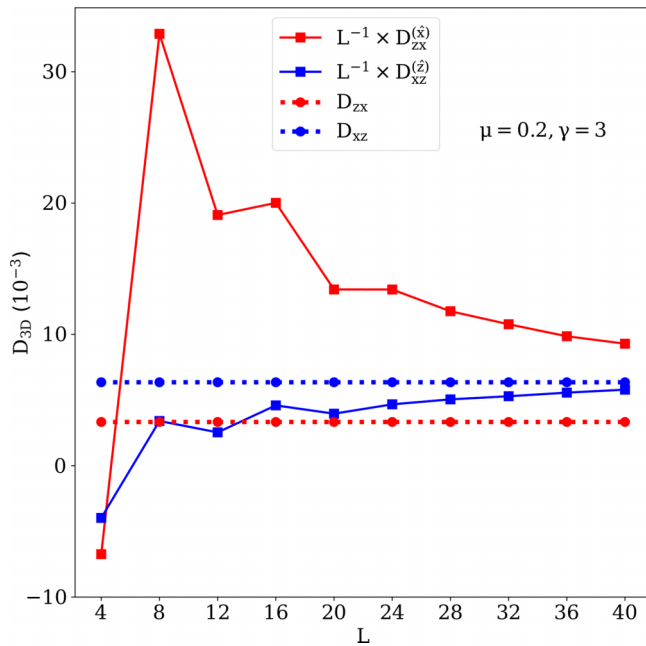

FIG. 6. Thickness dependence of the BCD in a type-II WSM for the $\hat{z}$ cut (blue) and $\hat{x}$ cut (red), as compared to the bulk values (dashed lines). The $\hat{x}$ cut shows a very strong deviation from the bulk value at small thicknesses, illustrating the importance of the surface states in this case.
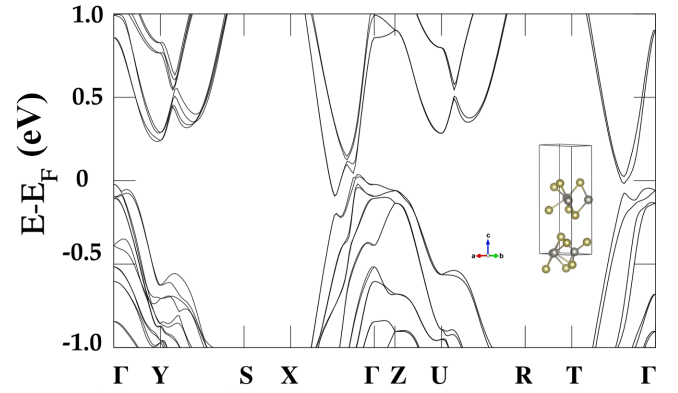

FIG. 7. Bulk band structure of WTe$_2$ type-II WSM obtained from density functional theory simulations. The inset displays the unit cell.

of 5 μev/Å and a reciprocal space sampling containing $16\times16\times14$ **k** points within the Brillouin zone. The ionic potentials were described using the projector augmented-wave (PAW) method [70], post-processing calculations were performed using WANNIERTOOLS [71]. The band structure is displayed in Fig. 7 with the inset showing the unit cell. The band crossings are located within the X-Γ path in momentum space, such that the Fermi level was set to zero near this region. With this consideration, we can project the Weyl points on selected surfaces, i.e., $\hat{z}$ [corresponding to the (001) direction] and $\hat{x}$ [corresponding to the (100) direction].

Let us first look at the density of states in the bulk and at the surface. Figure 8 displays the projected density of states in the bulk [(a)–(c)] and at the surface [(b)–(d)] for a slab cut along the $\hat{z}$ direction [(a) and (b)] and for a slab cut along the $\hat{x}$ direction [(c) and (d)]. As can be observed from Figs. 8(a) and 8(b), in the $\hat{z}$ cut the resulting density of states of the slab is larger at the surface than in the bulk, especially near the origin ($\bar{\Gamma}$ point). On the other hand, the opposite situation happens when the slab is normal to $\hat{x}$, as can be noticed from Figs. 8(c) and 8(d). From these results and comparing to the lattice model in Fig. 3, we deduce that the surface states highlighted in Fig. 8(b) should enhance the value of the BCD for the slab normal to $\hat{z}$, being strongly dependent on the thickness of the slab, whereas the geometry normal to $\hat{x}$ should be less sensitive to the Fermi arc diversity on the sample.

We now move on to the computation of the surface contribution of the NLHE for the two cuts considered above. For the calculation of the BCD, we have used Eq. (3) performing the sum over a sample Brillouin zone containing 500×500 k points. Figures 9(a) and 9(b) display the band structure and the BCD, respectively, computed for a slab cut along the $\hat{z}$ direction. The color bar in (a) represents the projections on the top and bottom surfaces of a slab containing 25 layers. One can distinguish both surfaces by the dark and yellow lines near the Fermi level. In panel (b), the BCD is computed as a function of the energy for slabs containing an increasing number of layers, from 15 to 25. It is clear that the energy profile of the BCD strikingly depends on the slab thickness. This thickness dependence reflects the influence of the surface states. For the sake of comparison, we also reported the value of the BCD computed in the bulk (dashed line). For an infinitely thick slab, the peaks present below the Fermi level and associated
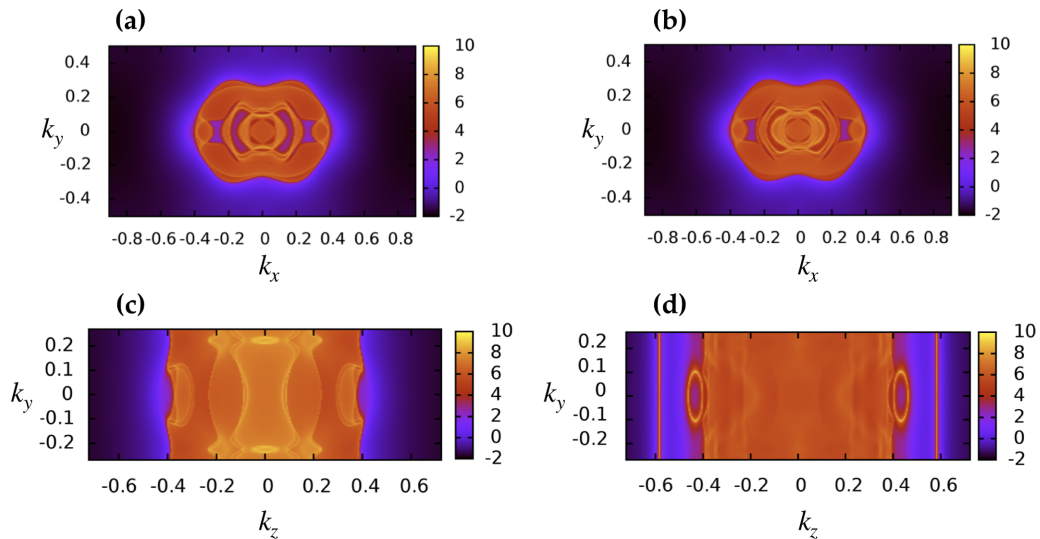
FIG. 8. WTe$_2$ density of states at Fermi level, projected on the bulk [(a) and (c)] and top surfaces [(b) and (d)] for a slab geometry containing 25 layers. (a) and (b) correspond to a cut along $\hat{z}$ whereas (c) and (d) correspond to a cut along $\hat{x}$.

with the surface states disappear. Similarly, Figs. 9(c) and 9(d) display the band structure and BCD, respectively, calculated for a slab cut along the $\hat{x}$ direction. In contrast to the $\hat{z}$ cut discussed above, the surface states cannot be clearly identified in the band structure that is instead dominated by bulk states. In panel (d), the BCD is computed for three different slab thicknesses. Interestingly, the qualitative behavior of the BCD is similar, displaying a peak whose position is weakly influenced by the slab thickness. For an infinitely thick slab, the bulk BCD (dashed line) conserves the overall structure, with
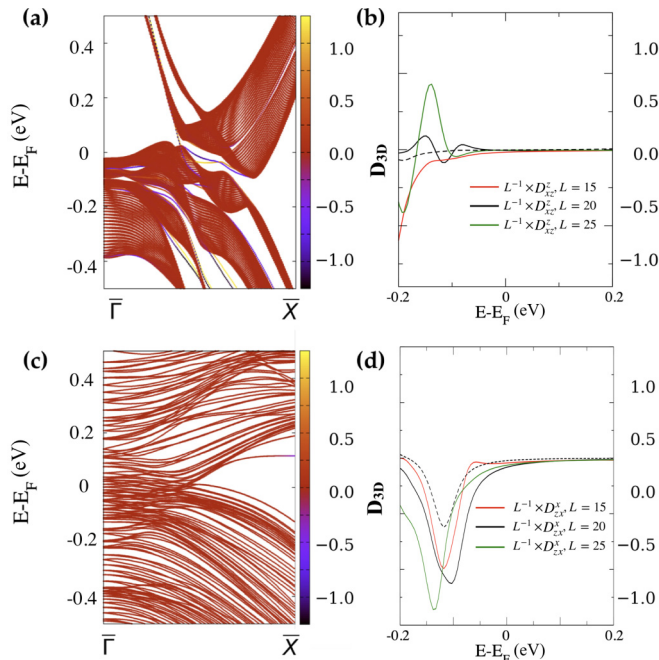
a slight reduction in magnitude. These calculations show that surface states do substantially impact the NLHE in realistic materials. An analogous behavior is obtained for the minimal model in the type-II regime ($\gamma = 3$), see Appendix B.

V. CONCLUSIONS

We have investigated the influence of surface states on the NLHE response of noncentrosymmetric time-reversal invariant WSMs. Using both a model Hamiltonian and realistic first principles calculations, we have demonstrated that depending on the direction of the cut, surface states emerge that can substantially contribute to the NLHE of the slab. Notice that the topological nature of the surface state (topologically protected arcs, or track states) has no impact on the overall BCD, only the relative number of states occupying the surface and the bulk matters. We emphasize that the relative contribution of the surface states with respect to the bulk states is in fact very large, leading to dramatic thickness-dependence of the NLHE response, in particular in type-II WSMs. This observation, confirmed by first principles calculations on WTe$_2$ slab geometries, suggests that surface states can contribute much more efficiently to NLHE than their bulk counterpart. We expect that the experimental signature of the surface-driven NLHE can be identified upon varying WSMs film thickness, depending on the growth orientation of the slab. These conclusions are not limited to WSMs and should apply to other topological systems and topologically trivial classes of noncentrosymmetric materials.

FIG. 9. Band structure of a WTe$_2$ slab containing 25 layers and cut along $\hat{z}$ (a) and $\hat{x}$ (c). For this case the color bar represents the projections on the bottom (-1) and top ($+1$) layers. [(b) and (d)] Corresponding BCD for bulk and slabs containing 15, 20, and 25 layers.
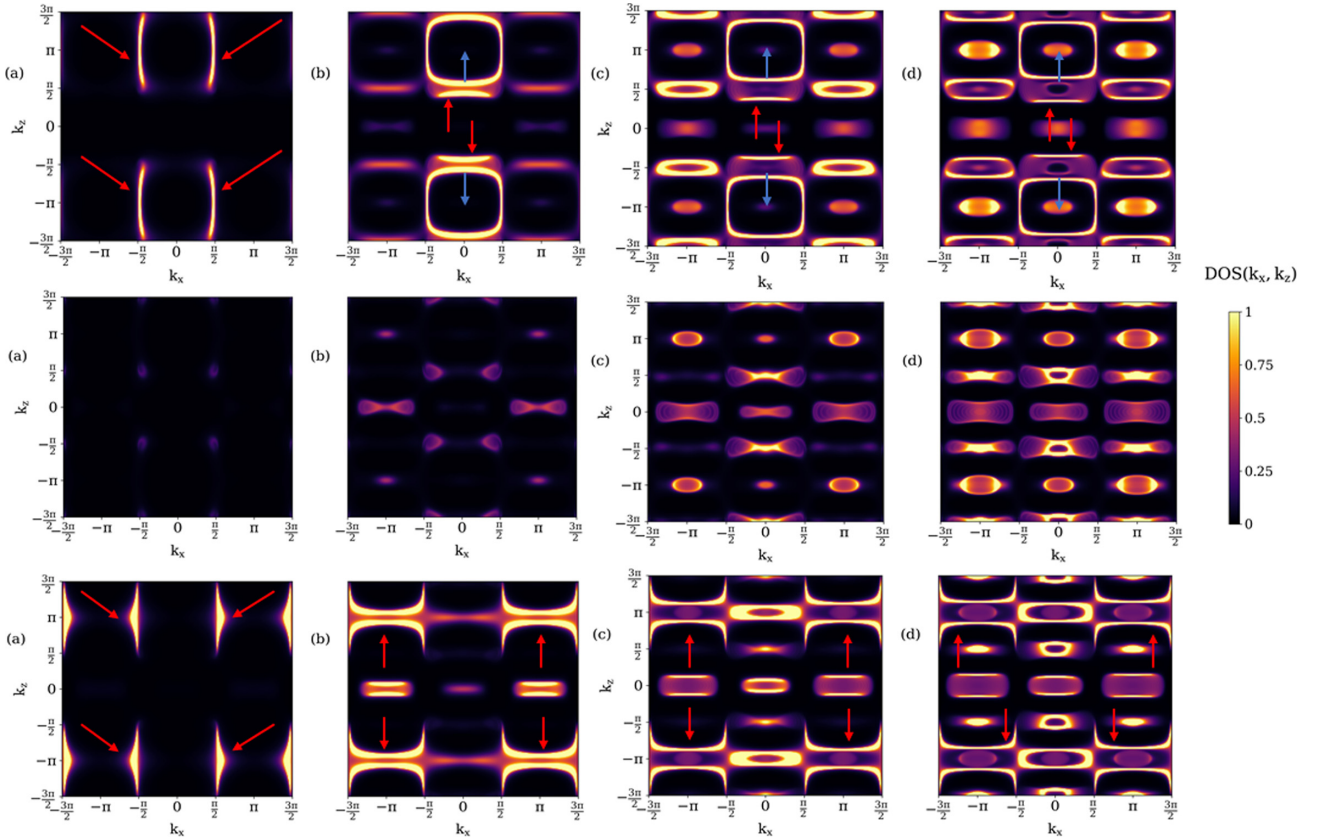
FIG. 10. Layer-resolved density of states of the topmost (top panels), central (middle panels) and bottommost (bottom panels) surface of a system with 25 layers and $\mu = 0.2$. The red arrows indicate the Fermi arcs, and the blue arrows point to the center of the track states. Finally, indexes (a)–(d) show the cases $\gamma = 1, \ 2, \ 2.5, \ 3$, respectively, i.e., tracking the transition from type-I to type-II WSM. The mismatch between the top and bottom surfaces is in agreement to what is reported in [51], and we assign this behavior to the absence of mirror symmetry along $\hat{y}$ in the original Hamiltonian given by Eq. (4).

APPENDIX A: FERMI ARCS RECONNECTION UPON TILTING

When transiting from type-I to type-II WSM, increasing the tilting of the Weyl cones induces a reconnection of the Fermi arcs. This is clearly observed in the y cut, as reported on Fig. 10. We observe a clear transition from Fermi arcs to Fermi pockets on the surface states (top and bottom panels). Indeed, a strong tilting can severely enlarge the Fermi pockets surrounding the Weyl nodes, leading to the merging between them and the generation of a trivial pocket. This is in fact what is happening at $\gamma = 3$ in Fig. 3(d). In other words, if one increases the tilting of the Weyl cones, the connectivity of the Fermi arcs is modified and can even induce the emergence of a trivial Fermi pocket from the merging of two Fermi pockets surrounding two opposite nodes.

APPENDIX B: DEPENDENCE ON THE FERMI LEVEL

All our calculations were performed away from the neutrality point, for $\mu = 0.2$. One might wonder how the Fermi level impact the relative contribution of the surface states and the bulk states to the NLHE. In Fig. 11, we show the dependence of the BCD as a function of the Fermi level for the [(a) and (c)] x and [(b) and (d)] z cut, for type-I ($\gamma = 1$) and type-II ($\gamma = 3$) WSM. We find that the scenario proposed in the main text qualitatively holds: the x
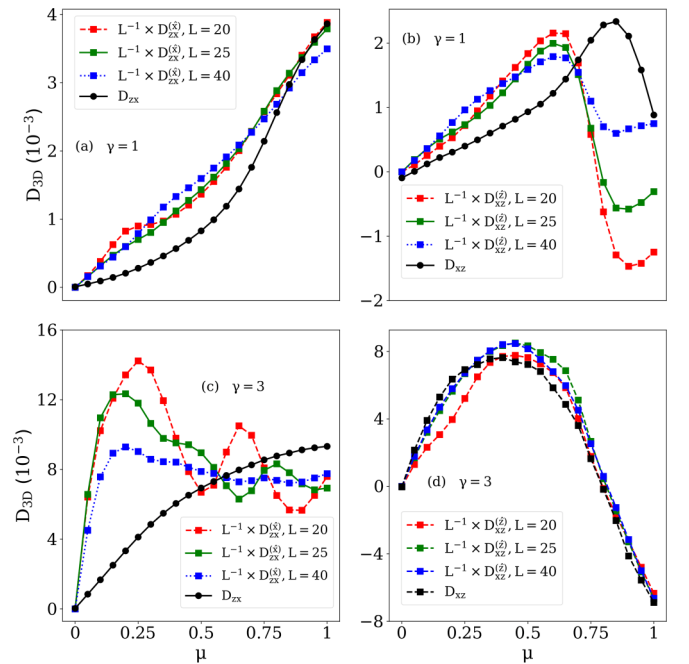

FIG. 11. Dependence of the BCD as a function of the chemical potential for the [(a) and (c)] x cut and [(b) and (d)] z cut, for type-I ($\gamma = 1$) and type-II ($\gamma = 3$) WSM.

cut, which possesses a strong surface contribution, exhibits a very strong difference between bulk BCD and slab BCD, regardless of the Fermi level, contrary to the z cut whose surface states are much less prominent. This effect is similar to that observed in the realistic calculations of WTe_2, see Fig. 9.

[1] E. Hall, On a new action of the magnet on electric currents, Am. J. Math. **2**, 287 (1879).

[2] E. Hall, On the "Rotational Coefficient" in nickel and cobalt, Philos. Mag. Ser. 5 **12**, 157 (1881).

[3] N. Nagaosa, J. Sinova, S. Onoda, A. H. MacDonald, and N. P. Ong, Anomalous Hall effect, Rev. Mod. Phys. **82**, 1539 (2010).

[4] H. Chen, Q. Niu, and A. H. MacDonald, Anomalous Hall Effect Arising from Noncollinear Antiferromagnetism, Phys. Rev. Lett. **112**, 017205 (2014).

[5] J. Kübler and C. Felser, Non-collinear antiferromagnets and the anomalous Hall effect, Europhys. Lett. **108**, 67001 (2014).

[6] S. Nakatsuji, N. Kiyohara, and T. Higo, Large anomalous Hall effect in a non-collinear antiferromagnet at room temperature, Nature (London) **527**, 212 (2015).

[7] A. K. Nayak, J. E. Fischer, B. Y. Yan Sun, J. Karel, A. C. Komarek, C. Shekhar, N. Kumar, W. Schnelle, J. Kübler, S. S. P. Parkin, and C. Felser, Large anomalous Hall effect driven by a non-vanishing Berry curvature in non-collinear antiferromagnet Mn_3Ge, Sci. Adv. **2**, 1501870 (2016).

[8] V. Bonbien, F. Zhuo, A. Salimath, O. Ly, A. Abbout, and A. Manchon, Topological aspects of antiferromagnets, J. Phys. D **55**, 103002 (2022).

[9] I. Sodemann and L. Fu, Quantum Nonlinear Hall Effect Induced by Berry Curvature Dipole in Time-Reversal Invariant Materials, Phys. Rev. Lett. **115**, 216806 (2015).

[10] Q. Ma, S.-Y. Xu, H. Shen, D. MacNeill, V. Fatemi, T.-R. Chang, A. M. Mier Valdivia, S. Wu, Z. Du, C.-H. Hsu, S. Fang, Q. D. Gibson, K. Watanabe, T. Taniguchi, R. J. Cava, E. Kaxiras, H.-Z. Lu, H. Lin, L. Fu, N. Gedik *et al.*, Observation of the nonlinear Hall effect under time-reversal-symmetric conditions, Nature (London) **565**, 337 (2019).

[11] K. Kang, T. Li, E. Sohn, J. Shan, and K. F. Mak, Nonlinear anomalous Hall effect in few-layer WTe_2, Nat. Mater. **18**, 324 (2019).

[12] D.-F. Shao, S.-H. Zhang, G. Gurung, W. Yang, and E. Y. Tsymbal, Nonlinear Anomalous Hall Effect for Néel Vector Detection, Phys. Rev. Lett. **124**, 067203 (2020).

[13] Z. Z. Du, C. M. Wang, H. P. Sun, H. Z. Lu, and X. C. Xie, Quantum theory of the nonlinear Hall effect, Nat. Commun. **12**, 5038 (2021).

[14] S. Nandy and I. Sodemann, Symmetry and quantum kinetics of the nonlinear Hall effect, Phys. Rev. B **100**, 195117 (2019).

[15] Z. Z. Du, C. M. Wang, H.-Z. Lu, and X. C. Xie, Band signatures for strong nonlinear Hall effect in bilayer WTe_2, Phys. Rev. Lett. **121**, 266601 (2018).

[16] J.-S. You, S. Fang, S.-Y. Xu, E. Kaxiras, and T. Low, Berry curvature dipole current in the transition metal dichalcogenides family, Phys. Rev. B **98**, 121109(R) (2018).

[17] Z. He and H. Weng, Giant nonlinear Hall effect in twisted bilayer WTe_2, npj Quantum Mater. **6**, 101 (2021).

[18] S. Singh, J. Kim, K. M. Rabe, and D. Vanderbilt, Engineering Weyl Phases and Nonlinear Hall Effects in t_d-$MoTe_2$, Phys. Rev. Lett. **125**, 046402 (2020).

[19] Y. Zhang, J. van den Brink, C. Felser, and B. Yan, Electrically tuneable nonlinear anomalous Hall effect in two-dimensional transition-metal dichalcogenides WTe_2 and $MoTe_2$, 2D Mater. **5**, 044001 (2018).

[20] B. T. Zhou, C.-P. Zhang, and K. T. Law, Highly tunable nonlinear Hall effects induced by spin-orbit couplings in strained polar transition-metal dichalcogenides, Phys. Rev. Appl. **13**, 024053 (2020).

[21] R. Battilomo, N. Scopigno, and C. Ortix, Berry Curvature Dipole in Strained Graphene: A Fermi Surface Warping Effect, Phys. Rev. Lett. **123**, 196403 (2019).

[22] P. A. Pantaleón, T. Low, and F. Guinea, Tunable large berry dipole in strained twisted bilayer graphene, Phys. Rev. B **103**, 205403 (2021).

[23] C.-P. Zhang, J. Xiao, B. T. Zhou, J.-X. Hu, Y.-M. Xie, B. Yan, and K. T. Law, Giant nonlinear Hall effect in strained twisted bilayer graphene, arXiv:2010.08333.

[24] S. S. Samal, S. Nandy, and K. Saha, Nonlinear transport without spin-orbit coupling or warping in two-dimensional dirac semimetals, Phys. Rev. B **103**, L201202 (2021).

[25] C. Zeng, S. Nandy, and S. Tewari, Nonlinear transport in Weyl semimetals induced by berry curvature dipole, Phys. Rev. B **103**, 245119 (2021).

[26] J. I. Facio, D. Efremov, K. Koepernik, J.-S. You, I. Sodemann, and J. van den Brink, Strongly Enhanced Berry Dipole at Topological Phase Transitions in BiTeI, Phys. Rev. Lett. **121**, 246403 (2018).

[27] Y. Zhang, Y. Sun, and B. Yan, Berry curvature dipole in Weyl semimetal materials: An *ab initio* study, Phys. Rev. B **97**, 041101(R) (2018).

[28] Y. Gao, F. Zhang, and W. Zhang, Second-order nonlinear Hall effect in Weyl semimetals, Phys. Rev. B **102**, 245116 (2020).

[29] T. Morimoto, S. Zhong, J. Orenstein, and J. E. Moore, Semiclassical theory of nonlinear magneto-optical responses with applications to topological dirac/Weyl semimetals, Phys. Rev. B **94**, 245121 (2016).

[30] H. Rostami and M. Polini, Nonlinear anomalous photocurrents in Weyl semimetals, Phys. Rev. B **97**, 195151 (2018).

[31] X. Wan, A. M. Turner, A. Vishwanath, and S. Y. Savrasov, Topological semimetal and Fermi-arc surface states in the electronic structure of pyrochlore iridates, Phys. Rev. B **83**, 205101 (2011).

[32] H. Nielsen and M. Ninomiya, The Adler-Bell-Jackiw anomaly and Weyl fermions in a crystal, Phys. Lett. B **130**, 389 (1983).

[33] N. P. Armitage, E. J. Mele, and A. Vishwanath, Weyl and dirac semimetals in three-dimensional solids, Rev. Mod. Phys. **90**, 015001 (2018).

[34] D. Rodriguez, A. A. Tsirlin, T. Biesner, T. Ueno, T. Takahashi, K. Kobayashi, M. Dressel, and E. Uykur, Two Linear Regimes in Optical Conductivity of a Type-I Weyl Semimetal: The Case of Elemental Tellurium, Phys. Rev. Lett. **124**, 136402 (2020).

[35] L. Meng, J. Wu, J. Zhong, and R. A. Römer, A type of robust superlattice type-I Weyl semimetal with four weyl nodes, Nanoscale **11**, 18358 (2019).

[36] B. Q. Lv, H. M. Weng, B. B. Fu, X. P. Wang, H. Miao, J. Ma, P. Richard, X. C. Huang, L. X. Zhao, G. F. Chen, Z. Fang, X.

Dai, T. Qian, and H. Ding, Experimental Discovery of Weyl Semimetal TaAs, Phys. Rev. X **5**, 031013 (2015).

[37] S.-Y. Xu, I. Belopolski, N. Alidoust, M. Neupane, G. Bian, C. Zhang, R. Sankar, G. Chang, Z. Yuan, C.-C. Lee, S.-M. Huang, H. Zheng, J. Ma, D. S. Sanchez, B. Wang, A. Bansil, F. Chou, P. P. Shibayev, H. Lin, S. Jia *et al.*, Discovery of a Weyl fermion semimetal and topological fermi arcs, Science **349**, 613 (2015).

[38] Y. Sun, S.-C. Wu, and B. Yan, Topological surface states and fermi arcs of the noncentrosymmetric Weyl semimetals TaAs, TaP, NbAs, and NbP, Phys. Rev. B **92**, 115428 (2015).

[39] K. Deng, G. Wan, P. Deng, K. Zhang, S. Ding, E. Wang, M. Yan, H. Huang, H. Zhang, Z. Xu, J. Denlinger, A. Fedorov, H. Yang, W. Duan, H. Yao, Y. Wu, S. Fan, H. Zhang, X. Chen, and S. Zhou, Experimental observation of topological fermi arcs in type-II Weyl semimetal MoTe$_2$, Nat. Phys. **12**, 1105 (2016).

[40] A. Tamai, Q. S. Wu, I. Cucchi, F. Y. Bruno, S. Riccò, T. K. Kim, M. Hoesch, C. Barreteau, E. Giannini, C. Besnard, A. A. Soluyanov, and F. Baumberger, Fermi Arcs and their Topological Character in the Candidate Type-II Weyl Semimetal MoTe$_2$, Phys. Rev. X **6**, 031021 (2016).

[41] F. Y. Bruno, A. Tamai, Q. S. Wu, I. Cucchi, C. Barreteau, A. de la Torre, S. McKeown Walker, S. Riccó, Z. Wang, T. K. Kim, M. Hoesch, M. Shi, N. C. Plumb, E. Giannini, A. A. Soluyanov, and F. Baumberger, Observation of large topologically trivial fermi arcs in the candidate type-II Weyl semimetal WTe$_2$, Phys. Rev. B **94**, 121112(R) (2016).

[42] Y. Wu, D. Mou, N. H. Jo, K. Sun, L. Huang, S. L. Bud'ko, P. C. Canfield, and A. Kaminski, Observation of fermi arcs in the type-II Weyl semimetal candidate WTe$_2$, Phys. Rev. B **94**, 121113(R) (2016).

[43] S. N. Guin, P. Vir, Y. Zhang, N. Kumar, S. J. Watzman, C. Fu, E. Liu, K. Manna, W. Schnelle, J. Gooth, C. Shekhar, Y. Sun, and C. Felser, Zero-field nernst effect in a ferromagnetic kagome-lattice Weyl-semimetal Co$_3$Sn$_2$S$_2$, Adv. Mater. **31**, 1806622 (2019).

[44] N. Morali, R. Batabyal, P. K. Nag, E. Liu, Q. Xu, Y. Sun, B. Yan, C. Felser, N. Avraham, and H. Beidenkopf, Fermi-arc diversity on surface terminations of the magnetic Weyl semimetal Co$_3$Sn$_2$S$_2$, Science **365**, 1286 (2019).

[45] G. Li, Q. Xu, W. Shi, C. Fu, L. Jiao, M. E. Kamminga, M. Yu, H. Tüysüz, N. Kumar, V. Süß, R. Saha, A. K. Srivastava, S. Wirth, G. Auffermann, J. Gooth, S. Parkin, Y. Sun, E. Liu, and C. Felser, Surface states in bulk single crystal of topological semimetal Co$_3$Sn$_2$S$_2$ toward water oxidation, Sci. Adv. **5**, eaaw9867 (2019).

[46] Q. Wang, Y. Xu, R. Lou, Z. Liu, M. Li, Y. Huang, D. Shen, H. Weng, S. Wang, and H. Lei, Large intrinsic anomalous Hall effect in half-metallic ferromagnet Co$_3$Sn$_2$S$_2$ with magnetic Weyl fermions, Nat. Commun. **9**, 3681 (2018).

[47] Y. Okamura, S. Minami, Y. Kato, Y. Fujishiro, Y. Kaneko, J. Ikeda, J. Muramoto, R. Kaneko, K. Ueda, V. Kocsis, N. Kanazawa, Y. Taguchi, T. Koretsune, K. Fujiwara, A. Tsukazaki, R. Arita, Y. Tokura, and Y. Takahashi, Giant magneto-optical responses in magnetic weyl semimetal Co$_3$Sn$_2$S$_2$, Nat. Commun. **11**, 4619 (2020).

[48] J. Ikeda, K. Fujiwara, J. Shiogai, T. Seki, K. Nomura, K. Takanashi, and A. Tsukazaki, Critical thickness for the emergence of Weyl features in Co$_3$Sn$_2$S$_2$ thin films, Commun. Mater. **2**, 18 (2021).

[49] W. Meng, X. Zhang, T. He, L. Jin, X. Dai, Y. Liu, and G. Liu, Ternary compound HfCuP: An excellent weyl semimetal with the coexistence of type-I and type-II Weyl nodes, J. Adv. Res. **24**, 523 (2020).

[50] M. Zhang, Z. Yang, and G. Wang, Coexistence of type-I and type-II Weyl points in the weyl-semimetal OsC$_2$, J. Phys. Chem. C **122**, 3533 (2018).

[51] T. M. McCormick, I. Kimchi, and N. Trivedi, Minimal models for topological Weyl semimetals, Phys. Rev. B **95**, 075133 (2017).

[52] A. Johansson, J. Henk, and I. Mertig, Edelstein effect in Weyl semimetals, Phys. Rev. B **97**, 085417 (2018).

[53] A. Potter, I. Kimchi, and A. Vishwanath, Quantum oscillations from surface Fermi-arcs in Weyl and Dirac semi-metals, Nat. Commun. **5**, 5161 (2014).

[54] D. Bulmash and X. L. Qi, Quantum oscillations in Weyl and Dirac semimetal ultrathin films, Phys. Rev. B **93**, 081103(R) (2016).

[55] C. M. Wang, H. Z. Lu, and S. Q. Shen, Anomalous Phase Shift of Quantum Oscillations in 3D Topological Semimetals, Phys. Rev. Lett. **117**, 077201 (2016).

[56] P. J. W. Moll, N. L. Nair, T. Helm, A. C. Potter, I. Kimchi, A. Vishwanath, P. J. W. Moll, and J. G. Analytis, Transport evidence for Fermi-arc-mediated chirality transfer in the Dirac semimetal Cd$_3$As$_2$, Nature (London) **535**, 266 (2016).

[57] M. Breitkreiz and P. W. Brouwer, Large Contribution of Fermi Arcs to the Conductivity of Topological Metals, Phys. Rev. Lett. **123**, 066804 (2019).

[58] J. Chesta Lopez, L. E. F. Foa Torres, and A. S. Nunez, Multiterminal conductance at the surface of a weyl semimetal, Phys. Rev. B **97**, 125419 (2018).

[59] E. V. Gorbar, V. A. Miransky, I. A. Shovkovy, and P. O. Sukhachov, Chiral separation and chiral magnetic effects in a slab: The role of boundaries, Phys. Rev. B **92**, 245440 (2015).

[60] P. S. Alekseev, A. P. Dmitriev, I. V. Gornyi, V. Y. Kachorovskii, B. N. Narozhny, M. Schütt, and M. Titov, Magnetoresistance of compensated semimetals in confined geometries, Phys. Rev. B **95**, 165410 (2017).

[61] T. Schumann, L. Galletti, D. A. Kealhofer, H. Kim, M. Goyal, and S. Stemmer, Observation of the Quantum Hall Effect in Confined Films of the Three-Dimensional Dirac Semimetal Cd$_3$As$_2$, Phys. Rev. Lett. **120**, 016801 (2018).

[62] D. Wawrzik, J.-S. You, J. I. Facio, J. van den Brink, and I. Sodemann, Infinite Berry Curvature of Weyl Fermi Arcs, Phys. Rev. Lett. **127**, 056601 (2021).

[63] G. Manchon, S. Ghosh, C. Barreteau, and A. Manchon, Semirealistic tight-binding model for spin-orbit torques, Phys. Rev. B **101**, 174423 (2020).

[64] P. Hohenberg and W. Kohn, Inhomogeneous electron gas, Phys. Rev. **136**, B864 (1964).

[65] W. Kohn and L. J. Sham, Self-consistent equations including exchange and correlation effects, Phys. Rev. **140**, A1133 (1965).

[66] J. P. Perdew, J. A. Chevary, S. H. Vosko, K. A. Jackson, M. R. Pederson, D. J. Singh, and C. Fiolhais, Atoms, molecules, solids, and surfaces: Applications of the generalized gradient approximation for exchange and correlation, Phys. Rev. B **46**, 6671 (1992).

[67] J. P. Perdew, K. Burke, and M. Ernzerhof, Generalized Gradient Approximation Made Simple, Phys. Rev. Lett. **77**, 3865 (1996).

[68] G. Kresse and J. Furthmüller, Efficiency of *ab-initio* total energy calculations for metals and semiconductors using a plane-wave basis set, Comput. Mater. Sci. **6**, 15 (1996).

[69] G. Kresse and J. Furthmüller, Efficient iterative schemes for *ab initio* total-energy calculations using a plane-wave basis set, Phys. Rev. B **54**, 11169 (1996).

[70] G. Kresse and D. Joubert, From ultrasoft pseudopotentials to the projector augmented-wave method, Phys. Rev. B **59**, 1758 (1999).

[71] Q. Wu, S. Zhang, H.-F. Song, M. Troyer, and A. A. Soluyanov, Wanniertools: An open-source software package for novel topological materials, Comput. Phys. Commun. **224**, 405 (2018).